

Geophysical Research Letters®



RESEARCH LETTER

10.1029/2023GL108018

Key Points:

- Teleseismic P-wave sources in the secondary microseismic band are inferred from a hindcast oceanographic model
- Seismic interferometry methods are applied to a “weather bomb” event between 8 and 11 December 2014 using an adaptive station pair selection
- Three-hour synthetic cross-correlation functions are compared to data to assess the impact of continuously varying sources on travel times

Supporting Information:

Supporting Information may be found in the online version of this article.

Correspondence to:

L. Tomasetto,
lisa.tomasetto@univ-grenoble-alpes.fr

Citation:

Tomasetto, L., Boué, P., Stehly, L., Arduin, F., & Nataf, H.-C. (2024). On the stability of mantle-sensitive P-wave interference during a secondary microseismic event. *Geophysical Research Letters*, 51, e2023GL108018. <https://doi.org/10.1029/2023GL108018>

Received 7 JAN 2024

Accepted 8 APR 2024

Author Contributions:

Conceptualization: L. Tomasetto, P. Boué

Data curation: L. Tomasetto

Formal analysis: L. Tomasetto

Funding acquisition: P. Boué

Investigation: L. Tomasetto

Methodology: L. Tomasetto, P. Boué

Project administration: P. Boué

Resources: F. Arduin

Software: L. Tomasetto, P. Boué, L. Stehly

Supervision: P. Boué, L. Stehly

Validation: L. Tomasetto, P. Boué, L. Stehly

Visualization: L. Tomasetto, P. Boué, L. Stehly, F. Arduin, H.-C. Nataf

© 2024. The Authors.

This is an open access article under the terms of the [Creative Commons Attribution License](#), which permits use, distribution and reproduction in any medium, provided the original work is properly cited.

On the Stability of Mantle-Sensitive P-Wave Interference During a Secondary Microseismic Event

L. Tomasetto¹ , P. Boué¹ , L. Stehly¹, F. Arduin² , and H.-C. Nataf¹
¹CNRS, IRD, Université Gustave Eiffel, Université Grenoble Alpes, University of Savoie Mont Blanc, Grenoble, France,

²Laboratoire d’Océanographie Physique et Spatiale, CNRS, IFREMER, IRD, University of Brest, Brest, France

Abstract Body wave extraction from oceanic secondary microseismic sources with seismic interferometry provides alternative information to better constrain the Earth’s structure. However, sources’ spatiotemporal variations raise concerns about travel time measurement robustness. Therefore, we study the cross-correlations’ stability during a single oceanic event. This study focuses on 3 days of data and three seismic arrays’ combinations between 8 and 11 December 2014 during storm Alexandra, a “weather bomb” event in southern Greenland. We use the WAVEWATCH III hindcast to model P-wave noise sources and assess the impact of short-term source variations on cross-correlations. Model-based cross-correlations compared to data show coherent delays to reference 3D Earth models (~0–3 s) confirming the robustness of the source model which could explain minor travel time variations (≤1 s).

Plain Language Summary Ocean wave interactions are a significant source of constant seismic wave emissions, known as ambient noise. Methods using correlations between seismic recordings recently highlighted surface waves and, more importantly, body waves to extract properties of the Earth’s deep interior. These studies either use continuous recordings to infer medium properties, or focus on wave propagation from a specific storm. However, concerns about measurements can come from the broad oceanic source constantly changing in space and time. We model seismic recordings for 3 days during a powerful oceanic storm in southern Greenland, 8–11 December 2014, to assess the source variations’ impact on body wave arrival times. We then compare it to data and measure travel time lags. Our findings explain source-induced delays and also agree with the known structure of the Earth, with some differences. This tool could add body wave travel time measurements and uncertainties from interferometry to image our planet’s deep structures.

1. Introduction

Seismic tomography is essential to understand processes that shape our planet, especially when considering the Earth’s mantle, where current models demonstrate complex geodynamical systems, imposing constraints on mineral composition and thermodynamics (e.g., Lay et al., 1998; Ritsema & Lekić, 2020; Ritsema et al., 1999; Romanowicz, 2003). Well-resolved global seismic velocity models are generally derived from earthquake-generated normal modes occasionally combined with long-period surface wave dispersion and often coupled with teleseismic body wave travel times. The latter bears the shortest wavelength information, which provides crucial details to characterize major discontinuities and deep structures’ geometry (e.g., Fukao & Obayashi, 2013). Most models use S-waves travel times, sometimes associated with P-waves data sets (e.g., Durand et al., 2017; Hosseini et al., 2020; C. Li et al., 2008; Ritsema et al., 2011). However, the mantle’s illumination is heterogeneous, degrading image resolution in some areas, even when considering ray paths reflected several times at the surface of the globe (SS, SSS, ...) (e.g., Lai & Garnero, 2020; Zaroli et al., 2015). Here, we discuss the possibility of using body waves from oceanic storms to add new constraints to mantle imaging by partially overcoming limits imposed by the uneven distribution of earthquakes and seismic stations (Boué & Tomasetto, 2023).

Seismic interferometry (SI) is often reduced to ambient noise correlations between seismic stations (e.g., Nakata et al., 2019) that can be interpreted as an estimate of the elastodynamic Green’s Function (GF) (e.g., Shapiro & Campillo, 2004; Wapenaar & Fokkema, 2006). For this assumption to be valid, all eigenrays must completely sample the medium between the two sensors within the correlated background wavefield, which is challenging for body waves at large scales (e.g., L. Li, Boué, & Campillo, 2020; Ruigrok et al., 2008). Wapenaar and Fokkema (2006) showed that a uniform distribution of noise sources on the Earth’s surface can fulfill these assumptions, which is done in practice by averaging over time. With the help of a stationary phase argument,

Writing – original draft: L. Tomasetto,
P. Boué, L. Stehly

Writing – review & editing:
L. Tomasetto, P. Boué, L. Stehly,
F. Ardhuin, H.-C. Nataf

promising signals emerged from seismic ambient noise, showing similarities between cross-correlation functions (CCFs) and the GF. Therefore, body waves have been extracted for various targets from the crust to the inner core (e.g., Boué et al., 2013; Nishida, 2013; Poli et al., 2012; Retailleau et al., 2020; Tkalčić & Pham, 2018). However, when these assumptions are not fulfilled, body waves' travel times from noise correlations and earthquakes differ significantly (e.g., Kennett & Pham, 2018). Ambiguities in the robustness of measurements for imaging applications have been reported in the secondary microseismic frequency band (e.g., L. Li, Boué, Retailleau, & Campillo, 2020).

Otherwise, one can directly interpret the correlation of seismic recordings as a measurement of differential propagation times between two stations for a given dominant source, either using late coda or ambient noise sources (e.g., Pham et al., 2018; Tkalčić et al., 2020). Boué and Tomasetto (2023) took another look at the daylight imaging concept (Rickett & Claerbout, 1999) and proposed to use oceanic storms lasting a few hours instead of continuous noise records to observe deep Earth seismic propagation (e.g., Nishida & Takagi, 2016; Zhang et al., 2023).

This study aims to test the possibility of using oceanic storms to measure P-wave travel time between station pairs without assuming that CCFs provide the GF, but using them to measure differential travel times between phases. In particular, we evaluate how the source spatiotemporal variations affect travel time measurements during a single major microseismic event. First, we describe the overall workflow from oceanic hindcast to synthetic cross-correlations modeling. Then we apply this workflow to a major event, called a “weather bomb”, in southern Greenland 8–11 December 2014 (Nishida & Takagi, 2016). Finally, after correcting source effects, we compare our measurements with travel times computed in three-dimensional (3D) mantle models for three network pairs.

2. Adaptive Seismic Interferometry Workflow

This study aims to quantify the impact of short-term oceanic sources' variations on a particular teleseismic P-waves interference. Therefore, we compare data-based correlograms to synthetics, based on a secondary microseismic source hindcast. The main steps of the workflow shown in Figure 1 are:

1. A major oceanic event is selected among a catalog derived from P-wave microseismic source models (Nishida & Takagi, 2022; Zhang et al., 2023), and seismic stations are paired accordingly to target the PP-P interference.
2. Synthetic correlograms are computed using modeled secondary microseismic sources and Green's Functions calculated in a laterally homogeneous Earth.
3. Globally selected station data are processed following Boué and Tomasetto (2023), and cross-correlations are computed for each station pair.
4. A detailed comparison of the observed and modeled correlations is performed for three chosen network combinations every 3 hr. The source dynamic's effect is quantified and corrected in the P-wave interference travel time measurements, which are further compared to 3D mantle models.

In this article, we propose a synthetics-to-data comparison case study for a well-known event (Nishida & Takagi, 2016), the novelty of our approach resides in points II and IV of the workflow.

3. Case Study: A Major Weather Bomb Event

Both Nishida and Takagi (2022) and Zhang et al. (2023) provide catalogs of events radiating significant P-waves in the secondary microseismic period band (3–10 s). The receiver-function imaging study in Japan by Kato and Nishida (2023) recently showed such a catalog's value for imaging applications. We decided to probe a “weather bomb”, which occurred in southern Greenland from 8 to 11 December 2014. A “weather bomb” is defined as an extratropical surface cyclone with a central pressure dropping of 1 mbar per hour (Sanders & Gyakum, 1980). We selected one of the most energetic cyclones detected, known for having generated in addition to P-waves, SV, and SH-waves (Gerstoft & Bromirski, 2016; Nishida & Takagi, 2016). According to the pelagic event's location and the dominant seismic frequency range (0.1–0.34 Hz), the secondary microseismic mechanism seems the most probable source (e.g., Ardhuin et al., 2011). Focusing on a particular event allows us to illustrate the potential biases in delay measurements related to the oceanic storm trajectory on a P-wave interference.

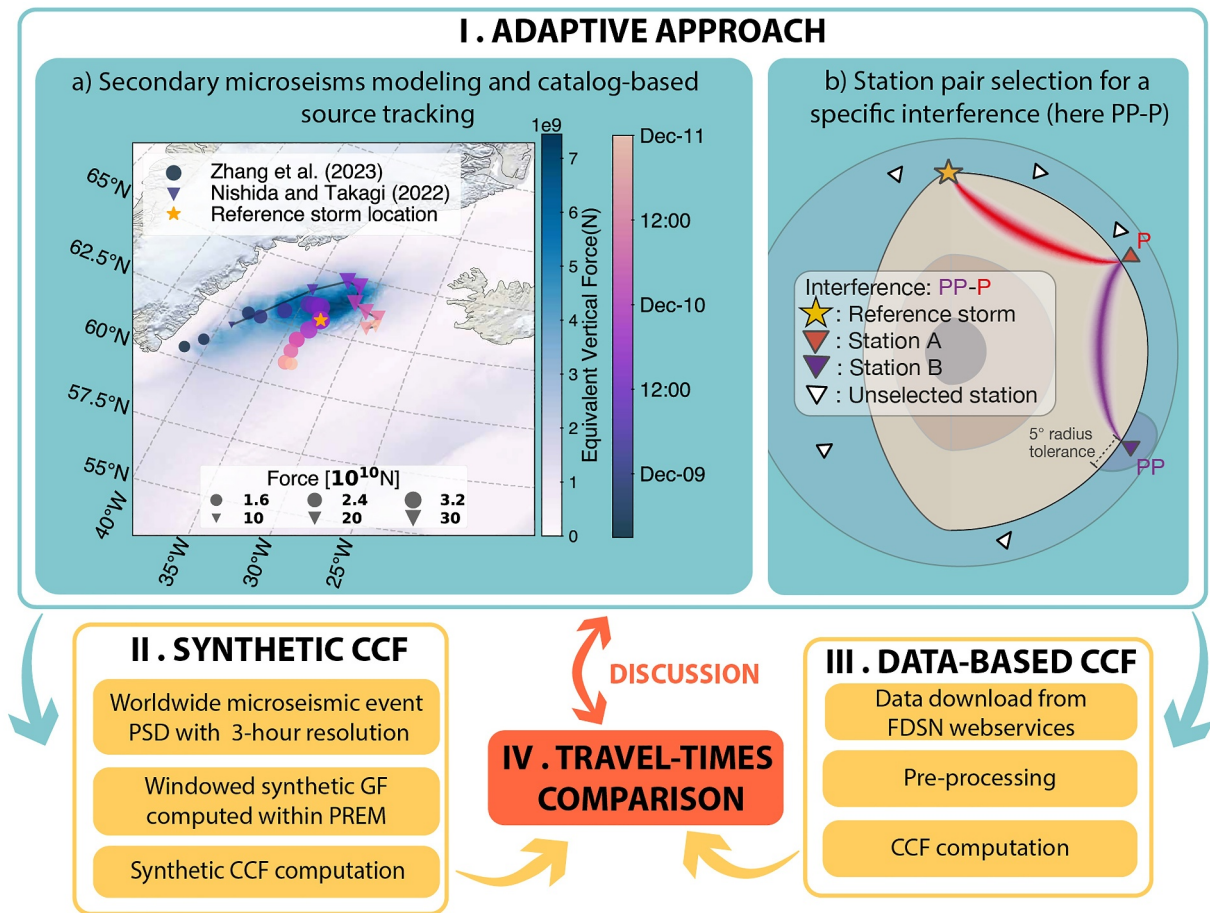


Figure 1. (I) Adaptive approach to a specific source. (a) Source modeling. Centroid positions from catalogs by Zhang et al. (2023) (circles) and back-projection centroid by Nishida and Takagi (2022) (triangles). The marker color and size represent the date and equivalent force, respectively. The reference location is indicated by the orange star (63°N, 33°W), and the background represents the equivalent vertical force on 9 December 2014 at 3 p.m. (b) Diagram explaining the station pairs selection for the PP-P interference. (II) Synthetic cross-correlation function computation using a dynamic source model within a 1D Earth model (III) Data pipeline counterpart in the 3–10 s period band (IV) Delay computation with a 3 hr resolution, and 3D models travel times comparison.

3.1. Network Combinations Selection

Following Boué and Tomasetto (2023), and knowing the event's trajectory from catalogs, shown in Figure 1a (Nishida & Takagi, 2022; Zhang et al., 2023), we select station pairs from the list of seismometers available via the International Federation of Digital Seismograph Networks (FDSN) to target the interference showing highest signal-to-noise ratio (SNR): PP-P. This interference, described in Figure 1b, highlights the travel time difference between a P-wave arriving at first station A and a PP-wave recorded at second station B. It emerges clearly above the noise level as it brings into play direct primary arrivals. By correlating signals of two seismic stations, one highlights travel time differences between recorded phases. For a given CCF averaged over the event's duration, a change in source position can lead to destructive interferences. Thus, we will rely on a stationary phase argument to measure travel times as insensitive as possible to source variations. In practice, this involves aligning the stations on a great circle containing the source and adjusting the relative source-receiver distances to the phases of interest (e.g., Pinzon-Rincon et al., 2021). We use ray approximation (Crotwell et al., 1999; Krischer et al., 2015), and PREM (Dziewonski & Anderson, 1981), to determine the optimum station pair positions. We first select all stations (A) possibly recording a direct P-wave emanating from the centroid position (63°N, 33°W). For each, we compute the coordinates of the optimal station B location by extending the ray trajectory following the same azimuth as a PP phase. Thus, this terminal point (optimal B location) lies twice the distance from the source to station A. However, Figure 1a shows that the source centroid evolves. So we allow a 5° radius around the terminal point to locate potential station B (see Figure 1b), estimated using reciprocity from the dimensions of the stationary phase zone on the source side.

3.2. Data Processing

Applying the previous geometrical selection, over 10,000 station pairs signals are downloaded (Figures 2a and 2b). Following Boué and Tomasetto (2023), we pre-process vertical components' data as follows: 3 hr window segmentation, resampling to 4 Hz and time synchronization, instrumental response deconvolution, and cross-coherence computation, which is a correlation normalized by the spectrum of both records. For representation purposes, the resulting CCFs are then summed over the whole event duration in 0.1° distance bins with the phase-weighted stack method (Schimmel & Paulssen, 1997). Figure 2b shows the causal part (propagation from the source toward the station pairs) of the stacked CCF, computed from 8 to 11 December 2014. CCFs are corrected and centered on the expected P-wave arrival time in PREM at an average distance. Emitted surface waves are dominant at short distances, blurring the weaker body wave signals (L. Li, Boué, Retailleau, & Campillo, 2020). So the PP-P interference emerges for inter-station distances larger than 20° . Yet subtle travel time fluctuations (~ 10 s) are observed along the distance axis, the overall stack (waveform on the right) shows a significant pulse around the average time of 509 s. These observed delays could indicate that the CCFs bear the Earth's structure signature, provided that the impact of source variations is insignificant. To confirm this, we select three subgroups of station pairs representing different distances and azimuths from the event (see Supporting Information S1). These subgroups correspond to correlations between networks GR-KO, KZ.KUR*-MY.KOM and ON-ZJ (2012–2015), shown respectively in red, yellow, and blue in Figures 2c–2e. For each station pair, we compute CCFs with a 3 hr sliding window and 30 min overlap over the event's duration. Then, we stack the CCFs belonging to the same subgroup to obtain a single average trace. Figures 2c–2e shows the average CCF for each subgroup. The PP-P interference appears in all three cases as a prominent pulse. GR-KO combination also shows a precursory P-P interference, which is expected for short interstation distances (e.g., Sager et al., 2020).

4. Modeling Cross-Correlation Functions in the Secondary Microseismic Band

Now that the stations' geometry is fixed, we quantify the source's trajectory impact on correlograms. Therefore, we generate synthetic CCFs computed within a laterally homogeneous model while integrating the P-wave microseismic source.

4.1. Secondary Microseismic Source

The secondary microseismic peak results from a non-linear interaction between similarly oscillating ocean waves moving in quasi opposite directions (e.g., Hasselmann, 1963; Longuet-Higgins, 1950). P-waves' radiation from these sources, in the 3–10 s period band, can be modeled using a sea state hindcast, the bathymetry, and a priori values of seismic velocities (Ardhuin et al., 2015; Gualtieri et al., 2014). We here follow a methodology discussed in Zhang et al. (2023) which modeled the distant P-wave seismic wavefield from a source model. The WW3 hindcast (WW3DG, 2019) accuracy to compute synthetic seismic motion has already been demonstrated for both surface and body waves (e.g., Ardhuin et al., 2011; Farra et al., 2016). Ardhuin et al. (2011) provides the spectral density of the pressure field at the sea surface F_p in $\text{Pa}^2 \text{m}^2 \text{s}$, with 0.5° spatial resolution in latitude and longitude and a 3 hr time step. To compare the event's spatiotemporal characteristics with previous studies, we compute the equivalent vertical force amplitude at the seabed (in N) from $f_{\min} = 0.10$ Hz to $f_{\max} = 0.34$ Hz.

$$F|_i(r) = 2\pi \sqrt{\int_{f_{\min}=0.10}^{f_{\max}=0.34} c_p^2(r, f) F_p|_i(r, f, K \approx 0) dA df} \quad (1)$$

with i the date index, $dA = R^2 \cos(\lambda) d\lambda d\phi$ the grid cell's surface, R the Earth's radius, λ the latitude and ϕ the longitude, K the sum of the two oceanic gravity waves' wavenumber, and f the seismic frequency, where

$$c_p(r, f) = \sqrt{\int_0^{\theta_{pw}^*} \left| \frac{T_p(\theta_{pw})}{1 + R(\theta_{pw}) e^{i\Phi_w(h(r), 2\pi f, \theta_{pw})}} \right|^2 d\theta_{pw}} \quad (2)$$

with h the ocean depth, θ_{pw} the P-wave takeoff angle, Φ_w plane P-wave potential propagating in water, R , and T are the seabed interface reflection and transmission coefficients, respectively.

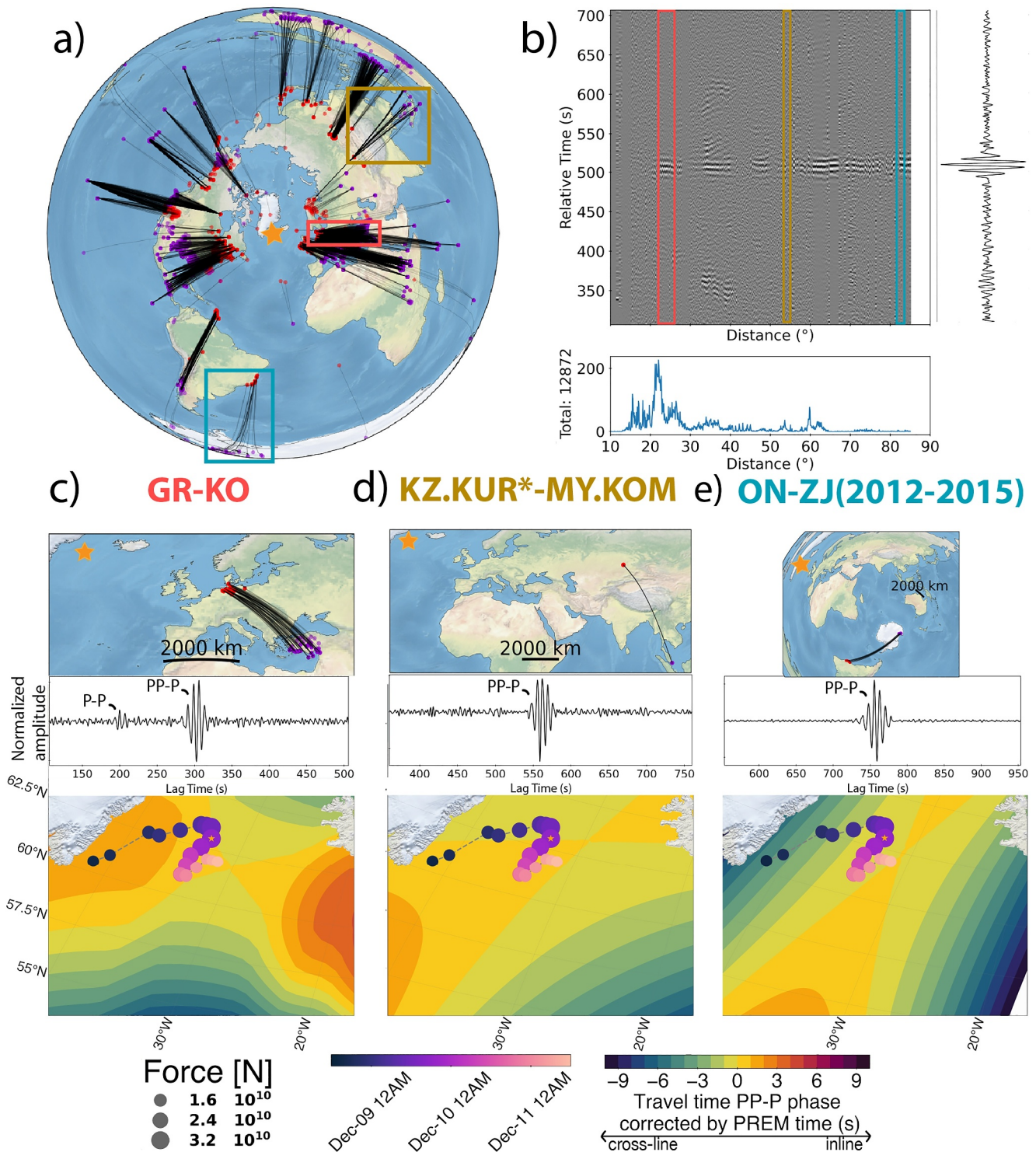


Figure 2. (a) Map of the event location (orange star) and corresponding station pairs selection (black lines) for the PP-P interference. Stations A and B are represented as red and purple dots, respectively. (b) The causal part of filtered cross-correlation functions (CCFs) reduced in time (i.e., centered on the P-wave arrival time at an average distance) and stacked. A histogram of CCF density is represented below. (c), (d), and (e) for each: (top) station paths from station A in red to station B in purple (middle) the stacked CCFs. (bottom) The event's centroid trajectory and its equivalent vertical force are shown upon isochrone contours.

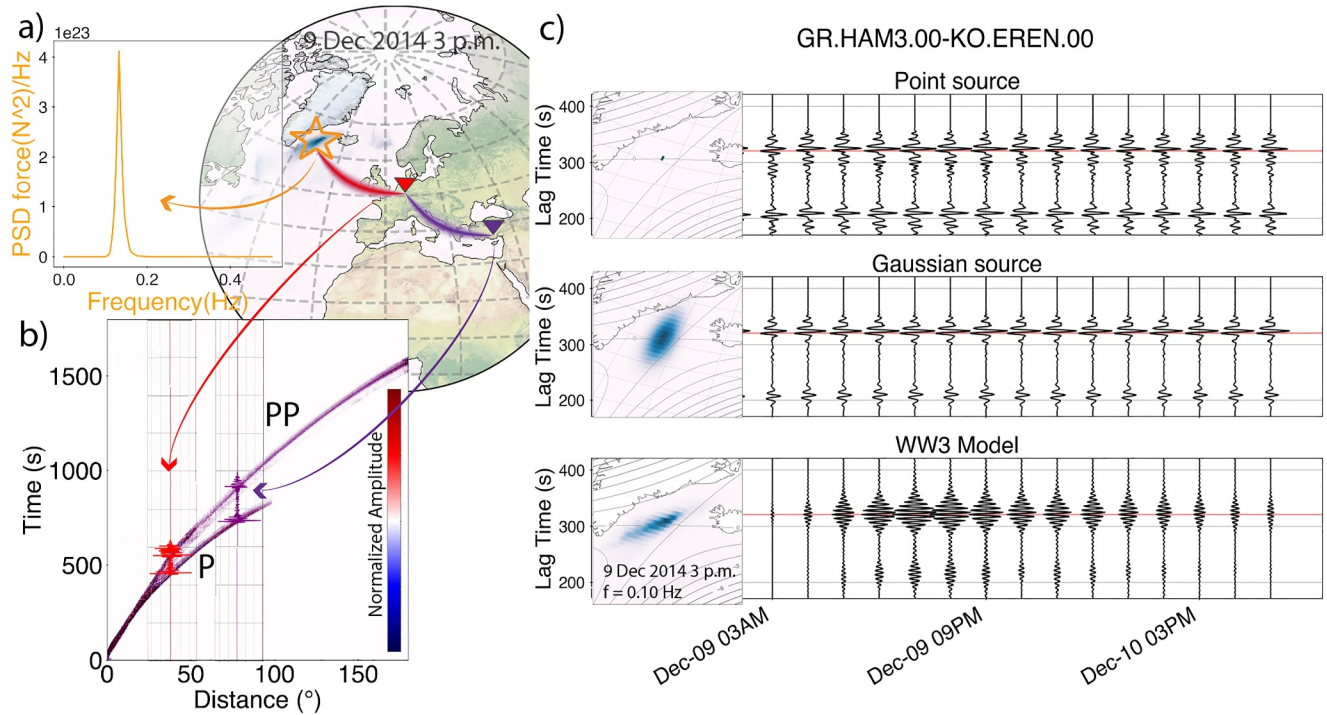


Figure 3. Cross-correlation functions (CCFs) modeling diagram. (a) Secondary microseismic source power spectral density from the WW3 model on 9 December 2014 at 3 p.m. at the reference location (63°N, 33°W). (b) GFs computed with AxiSEM windowed to target P and PP-waves only, and examples of waveforms at 40° and 80° in red and purple respectively. (c) Normalized synthetic CCFs for station pair (GR.HAM3-KO.EREN.00) using three different source distributions. From top to bottom, a point source and a Gaussian patch source, both following the weather bomb's trajectory, and the WW3 model ocean forcing. The red line is the P-wave arrival time in PREM.

Figure 1a shows the equivalent vertical force in southern Greenland on 9 December 2014 at 3 p.m. and the event's tracks given by Nishida and Takagi (2022) and Zhang et al. (2023). Discrepancies between the two tracks are explained by a typical precision of 150 km on the source location in Nishida and Takagi (2022). The value of 10^{10} N is consistent with previous studies (e.g., Vinnik, 1973). The force $F_l(r)$ helps track the spatiotemporal event behavior, while the ocean forcing $4\pi^2 c_p^2(r, f) F_p|_i(r, f)$ is used as the source frequency content for synthetic correlograms.

4.2. Synthetics Cross-Correlations

To generate synthetic correlograms we apply the formulation of Sager et al. (2022) to the spherical Earth and use the ocean-forcing as the source term. The CCF between vertical components recorded by two seismic sensors can be derived from the representation theorem in the frequency domain (Aki & Richards, 2002; Nakata et al., 2019). Assuming spatially uncorrelated sources (Ayala-Garcia et al., 2021), see Supporting Information S1. It can be written for each 3 hr date index i as:

$$C_i^{synth}(r_A, r_B, t) = \mathcal{FT}^{-1} \left[\int_{\partial D} G(r_A, r, f) G^*(r_B, r, f) S_i(r, f) dr \right] \quad (3)$$

With $G(r_A, r, f)$ the GF between a source in r and a sensor in r_A , $S_i(r, f) = 4\pi^2 c_p^2(r, f) F_p|_i(r, f) dA$ the power spectral density of the source at position r and $*$ the complex conjugate. ∂D corresponds to the oceans' surface, and \mathcal{FT}^{-1} to the inverse Fourier transform.

GFs are computed for a vertical point force within PREM with attenuation using AxiSEM (Nissen-Meyer et al., 2008), then filtered in the frequency band 0.08–0.4 Hz. They are further windowed around P and PP-wave arrivals, as shown in Figure 3b, to remove surface waves and other cross-terms not appearing in the data CCFs (e.g., Sager et al., 2022; Zhang et al., 2023). Since global 1D models smooth upper layers' heterogeneities,

surface wave scattering is underestimated leading to unrealistic attenuation simulation. Approaches using 3D wave propagation solvers in regional settings might explain the dominance of body waves in the CCF (e.g., Afanasiev et al., 2019; Nouibat et al., 2023). For global-scale applications, we chose to mute surface waves. Figure 3 illustrates the CCFs modeling. Panel (b) represents the synthetic windowed GF computed at 40° and 80° distance from the source in red and purple respectively. Figure 3c shows modeled CCFs between a station in Germany (GR.HAM3) and another in Turkey (KO.EREN) from 8 to 11 December 2014. To visualize the source extent's impact on synthetic correlations, we test three source distributions: a point source $\delta(t, r)$ and a 2° width Gaussian pulse, both centered on the event's centroid every 3 hr, shown in Figure 1a, and finally the ocean forcing $S(r, f)$. While the first two distributions present a flat spectrum in the 0.10–0.34 Hz band, the model distribution includes the source's frequency content at each grid point on the whole ocean's surface, as shown by Figure 3a. As their data counterparts, P-P and PP-P interferences emerge for all source distributions around 200 and 320 s respectively. The latter is highlighted by the red line in Figure 3c corresponding to the P-wave arrival time between stations, t_{PREM} . The first two source types have a constant spectral amplitude over time. Consequently, the small changes observed in the corresponding 3 hr correlations are due to the centroid trajectory. On the other hand, the model-based source distribution shows an increase in amplitude to its peak on 9 December at 3 p.m. that reduces progressively. The synthetic correlograms integrating realistic source models seem to show small travel time variations, which we quantify and compare to data in the following. As for the data counterpart, we compute synthetic CCF for each station pair and stack them to obtain one average CCF per subgroup.

5. Differential Travel Times Analysis

This section aims to assess whether P-wave travel times obtained from noise correlations computed during the event are accurate enough to be applied to tomography. First, we use a ray theory approach to estimate the expected delays due to the source dynamic on each subgroup geometry. Second, we introduce two ways to compare synthetics and data-based CCFs. The first one quantifies short-term variations imputable to the source by comparing waveforms to a reference trace. The second directly compares synthetics to data to measure propagation effects, which are then compared to 3D model counterparts.

5.1. Source Effect Estimation Using Ray Tracing: dt_{PREM}

We quantify the PP-P interference delay assuming that the source is a point source following the catalog's trajectory. For each network pair, we compute the barycenter locations of network A and network B. We evaluate the difference of travel time dt_{PREM} between the PP-P interference travel time, and the P-wave computed in PREM propagating between these two barycenters. We iterate over a grid of potential source points on the ocean surface (S) and for each compute dt_{PREM} as:

$$dt_{PREM}(S) = t_{PREM}^{PP}(SB) - t_{PREM}^P(SA) - t_{PREM} \quad (4)$$

where $t_{PREM}^{PP}(SB)$ is the PP-wave arrival time between the source and barycenter B, $t_{PREM}^P(SA)$ is the P-wave travel time between the source and barycenter A, and $t_{PREM} = t_{PREM}^P(AB)$ is the P-wave travel time between barycenter A and barycenter B. The resulting dt_{PREM} delay maps shown in Figures 2c–2e exhibit a saddle point shape typical of the PP-P interference (e.g., Sager et al., 2022), whose vicinity delimits the stationary phase area. The centroid trajectory from Zhang et al. (2023) is also mapped to estimate delays for each 3 hr window between 9 and 10 December 2014. For the three subgroups, we expect dt_{PREM} to be less than 1 s. The GR-KO subgroup should initially show a positive delay of around 1 s, converging toward zero (Figures 2c and 4b). The KZ.KUR*-MY. KOM subgroup should display small variations around zero due to the large stationary phase zone (Figures 2d and 4b). Finally, the ON-ZJ subgroup combination should present negative delays down to −1 s converging toward zero (Figures 2d and 4b). dt_{PREM} quantifies the error due to source variations on the PP-P interference every 3 hr.

5.2. Source Induced Delays: dt_{ref}

In this section, we evaluate how the source's spatiotemporal evolution affects observed and synthetic CCF. If the source modeling is well-constrained, the PP-P travel times evolution should be similar. Figure 4 shows the

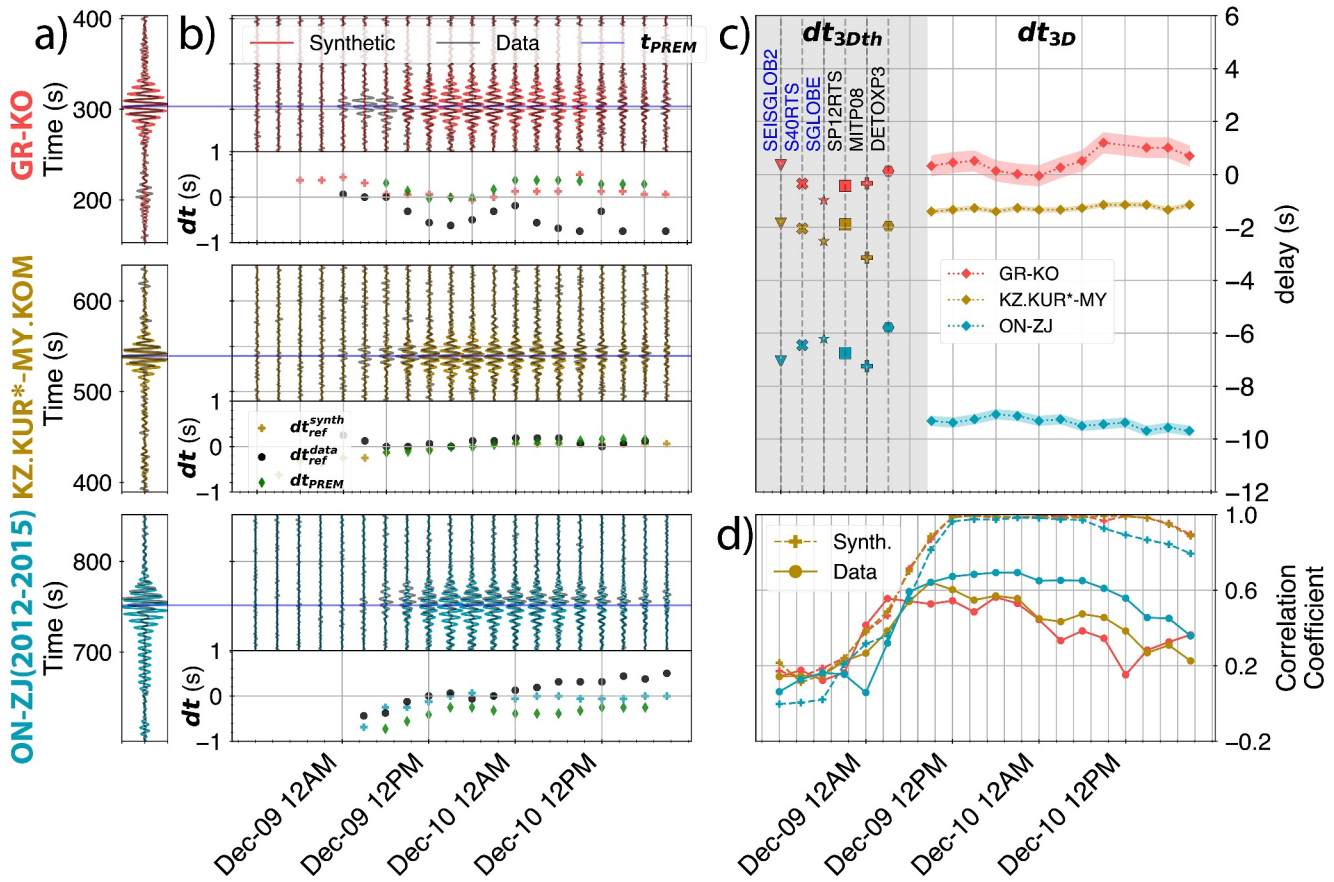


Figure 4. Synthetics (in color) and data-based (in black) cross-correlation functions (CCFs) comparison for GR-KO, KZ.KUR*-MY.KOM, ON-ZJ (2012–2015) respectively in red, yellow, and blue. (a) Average trace (b) Synthetics and data CCFs 8–11 December 2014. The inset for each subgroup shows dt_{PREM} (green diamonds) and time shifts between 3 hr and stacked windowed waveforms (dt_{ref}) for data (round points) and synthetics (crosses). (c) Cross-correlation-based timeshift between data and synthetic windowed waveforms dt_{3D} (diamonds) every 3 hr and their standard deviation. The left colored markers indicate delays computed using SeisTomoPy in 3D models dt_{3Dth} , P waves-based models names in black. (d) Correlation coefficient of synthetic and data waveforms to their respective average trace after correction of dt_{ref} .

comparison between data and synthetic CCFs, in black and bright colors, respectively. Figure 4a shows the average waveform for each subgroup (reference), windowed around t_{PREM} (blue line), and Figure 4b the equivalent for 3 hr time windows. Subgroups GR-KO, KZ.KUR*-MY.KOM, ON-ZJ (2012–2015) are in red, yellow, and blue respectively. At the bottom of each panel, an inset displays the cross-correlation timeshift between each 3 hr waveform and its average waveform windowed around t_{PREM} , named dt_{ref} .

$$dt_{ref}|_i^{data/synth} = \underset{t \in \mathbb{R}}{\operatorname{argmax}} \left(\left[C_i^{data/synth} \star \langle C_i^{data/synth} \rangle \right] (r_A, r_B, t) \right) \quad (5)$$

where i denotes the date index, $\langle \rangle$ the mean with date, and \star the correlation operator. We then compute the correlation coefficient between each 3 hr CCF corrected by dt_{ref} and the average CCF (Figure 4d) which indicates when the source is dominant and stable. The synthetic CCFs globally show a high correlation coefficient (≥ 0.9) from 9 December, 9 a.m. to 10 December, 6 a.m. The data however present lower correlation coefficients, oscillating around 0.5. The dt_{ref} exhibits short-time variations between -1 and 1 s. In particular, the ON-ZJ (2012–2015) sub-selection shows similar behavior for synthetic and data CCFs, with a negative delay converging toward zero. Otherwise, the GR-KO subgroup shows different delay evolutions which might be explained by the weak correlation coefficient due to a wide array aperture, summing heterogeneous paths. As expected, the KZ.KUR*-MY.KOM cross-correlations present delays close to zero for both data and synthetic CCFs. So the gap between the two curves estimates the source modeling accuracy for each 3 hr segment.

5.3. Toward a Robust Travel Time Estimation: dt_{3D}

Now that we evaluated the variability of the PP-P interference travel time due to the spatiotemporal evolution of the source, we aim to highlight delays that could be due to velocity anomalies in the Earth's mantle. We compute dt_{3D} , timeshifts between observed and synthetic waveforms every 3 hr based on cross-correlation, shown as diamond markers in Figure 4c.

$$dt_{3D}|_i = \underset{t \in \mathbb{R}}{\operatorname{argmax}} \left(\left(C_i^{\text{data}} \star C_i^{\text{synth}} \right) (r_A, r_B, t) \right) \quad (6)$$

Since the synthetic CCFs have been computed in a laterally homogeneous model, we assume this delay to be a measure of the travel time difference to PREM. We find mean delays of 0.51 s for GR-KO, -1.27 s for KZ.KUR*-MY.KOM and -9.38 s for ON-ZJ (2012–2015). Our measurements are compared to their travel time difference counterpart between PREM (1D) and 3D models, named dt_{3Dth} as:

$$dt_{3Dth} = t_{3D}^{PP}(SB) - t_{3D}^P(SA) - (t_{1D}^{PP}(SB) - t_{1D}^P(SA)) \quad (7)$$

Presented models inverting shear-wave velocity (SEISGLOB2 (Durand et al., 2017), S40RTS (Ritsema et al., 2011), SGLOBE (Chang et al., 2015)) or compressional-wave velocity (SP12RTS (Koelemeijer et al., 2016), MITP08 (C. Li et al., 2008) and DETOX-P3 (Hosseini et al., 2020)) are represented as colored markers in Figure 4c. The mean values of dt_{3Dth} are 0.13 s for GR-KO, and -2.25 s for KZ.KUR*-MY.KOM and -6.67 s for ON-ZJ (2012–2015), with ellipticity corrections applied (Durand et al., 2018) (details in Supporting Information S1). Finally, measured and computed travel times differ by 0.38 s for GR-KO, 0.98 s for KZ-MY and 2.71 s for ON-ZJ (2012–2015) which seems consistent with residuals found in earthquake body waves studies (e.g., Montelli et al., 2004; Zaroli et al., 2010). However, ON-ZJ (2012–2015) shows the most significant timeshifts and waveform differences, studying other paths in Antarctica could help discriminate this discrepancy with global models. Let us note that earthquake raypath coverage is poor under the oceans, therefore uncertainties of the tomographic models are larger (e.g., Durand et al., 2017; Romanowicz, 2003). This opens up the possibility of using simultaneously P-wave travel times from earthquakes and oceanic storms to image the deep Earth.

6. Discussion and Conclusion

This study investigated the potential of oceanic sources to measure teleseismic body wave velocities. To answer this question, we focused on a 3 days major oceanic event in the northern Atlantic Ocean to assess the stability of the PP-P interference measured between three sets of stations. We used the WW3 hindcast to model secondary microseismic sources and measure the travel times obtained from synthetic and observed CCFs. We quantify for each 3 hr time window the variability of these measurements due to the source's trajectory (dt_{PREM}) and modeling of the oceans' secondary microseismic sources (dt_{ref}). These variations remain small (± 1 s) compared to the propagation time of the direct P-waves (0.5% at most). Finally, for the three sets of stations, we show that PP-P travel times measured from the oceanic event and predicted by 3D models are coherent with each other. This suggests that oceanic storms could be used as a seismic source to measure body-waves travel time measurement with an unconventional ray coverage. These measurements could be added to existing data sets to better constrain tomographic images. However, a remaining study on the finite-frequency sensitivity kernels of the PP-P interference for an extended source must be included for future tomographic applications. At the regional scale, Sager et al. (2022) showed acute sensitivity near source and receiver locations for a punctual source that decreases for an extended source. Recent oceanic event catalogs identify more than 24,000 events from 2004 to 2022, leaving much data to decipher and possibly statistical approaches to these measurements. The next step would be to apply this method to all major oceanic events of the last 15 years to evaluate more precisely the potential of this method for seismic tomography. Smaller events could be stacked with the source effects formerly corrected to enhance the SNR of the CCF so that we could measure travel time anomalies on single station pairs instead of network combinations. Finally, this method could be used to explore other interferences, involving PKP or PcP phases. One could also imagine monitoring areas illuminated by recurrent microseismic sources (e.g., Sheng et al., 2022).

Conflict of Interest

The authors declare no conflicts of interest relevant to this study.

Data Availability Statement

Seismic waveforms are accessible via IRIS web services, in particular networks KZ (KNDC/Institute of Geophysical Research (Kazakhstan), 1994), MY (no DOI available but information can be found at <https://www.fdsn.org/networks/detail/MY/>), ON (Observatório Nacional, Rio de Janeiro, RJ, 2011) and ZJ (2012–2015) (Samantha, 2012). GR (Federal Institute for Geosciences and Natural Resources, 1976) can also be downloaded from BGR Hannover, and KO (Kandilli Observatory And Earthquake Research Institute, Boğaziçi University, 1971) through KOERI web service.

Listed here are the resources used in this study:

Data processing with PyCorr package, Boué and Stehly (2022).

The oceanographic hindcast WAVEWATCH III documentation can be accessed at <https://iowaga.ifremer.fr/Products>.

The ETOPOv2 bathymetry can be found on the National Center for Environmental Information, NOAA National Centers for Environmental Information (2022).

Travel times in 3D models using the SeisTomoPy package: Durand et al. (2018).

Ellipticity corrections with the EllipticiPy package: Russell et al. (2022).

Acknowledgments

This study is funded by the Agence Nationale de la Recherche (ANR) Grant ANR-CE49-0003. The authors thank Ruohan Zhang, who provided the catalog and codes for the P-wave microseismic sources modeling, and Stéphanie Durand for her advice on delay computation with SeisTomoPy and help to integrate P-wave dataset-based mantle models. We thank Daoyuan Sun, Thanh Son Pham, and another anonymous reviewer for their remarks that helped improve this manuscript. We also thank all seismologists and technical staff who enable access to global seismic data.

References

- Afanasiev, M., Boehm, C., van Driel, M., Krischer, L., Rietmann, M., May, D. A., et al. (2019). Modular and flexible spectral-element waveform modelling in two and three dimensions. *Geophysical Journal International*, 216(3), 1675–1692. <https://doi.org/10.1093/gji/ggy469>
- Aki, K., & Richards, P. G. (2002). Quantitative seismology.
- Arduhin, F., Gualtieri, L., & Stutzmann, E. (2015). How ocean waves rock the Earth: Two mechanisms explain microseisms with periods 3 to 300 s. *Geophysical Research Letters*, 42(3), 765–772. <https://doi.org/10.1002/2014GL062782>
- Arduhin, F., Stutzmann, E., Schimmel, M., & Mangeney, A. (2011). Ocean wave sources of seismic noise. *Journal of Geophysical Research*, 116(C9), C09004. <https://doi.org/10.1029/2011JC006952>
- Ayala-García, D., Curtis, A., & Branicki, M. (2021). Seismic interferometry from correlated noise sources. *Remote Sensing*, 13(14), 2703. <https://doi.org/10.3390/rs13142703>
- Boué, P., Poli, P., Campillo, M., Pedersen, H., Briand, X., & Roux, P. (2013). Teleseismic correlations of ambient seismic noise for deep global imaging of the Earth. *Geophysical Journal International*, 194(2), 844–848. <https://doi.org/10.1093/gji/ggt160>
- Boué, P., & Stehly, L. (2022). Pycorr [Software]. Zenodo. <https://doi.org/10.5281/zenodo.6793401>
- Boué, P., & Tomasetto, L. (2023). Opportune detections of global P-wave propagation from microseisms interferometry. *Comptes Rendus Geoscience*, 355(S3), 1–16. <https://doi.org/10.5802/crgeos.222>
- Chang, S.-J., Ferreira, A. M., Ritsema, J., van Heijst, H. J., & Woodhouse, J. H. (2015). Joint inversion for global isotropic and radially anisotropic mantle structure including crustal thickness perturbations. *Journal of Geophysical Research*, 120(6), 4278–4300. <https://doi.org/10.1002/2014JB011824>
- Crotwell, H. P., Owens, T. J., & Ritsema, J. (1999). The TauP Toolkit: Flexible seismic travel-time and ray-path utilities. *Seismological Research Letters*, 70(2), 154–160. <https://doi.org/10.1785/gssrl.70.2.154>
- Durand, S., Abreu, R., & Thomas, C. (2018). Seistomopy: Fast visualization, comparison, and calculations in global tomographic models. *Seismological Research Letters*, 89(2A), 658–667. <https://doi.org/10.1785/0220170142>
- Durand, S., Debayle, E., Ricard, Y., Zanolli, C., & Lambotte, S. (2017). Confirmation of a change in the global shear velocity pattern at around 1000 km depth. *Geophysical Journal International*, 211(3), 1628–1639. <https://doi.org/10.1093/gji/ggx405>
- Dziewonski, A. M., & Anderson, D. L. (1981). Preliminary reference Earth model. *Physics of the Earth and Planetary Interiors*, 25(4), 297–356. [https://doi.org/10.1016/0031-9201\(81\)90046-7](https://doi.org/10.1016/0031-9201(81)90046-7)
- Farra, V., Stutzmann, E., Gualtieri, L., Schimmel, M., & Arduhin, F. (2016). Ray-theoretical modeling of secondary microseism P waves. *Geophysical Journal International*, 206(3), 1730–1739. <https://doi.org/10.1093/gji/ggw242>
- Federal Institute for Geosciences and Natural Resources. (1976). German regional seismic network (GRSN) [Dataset]. *Bundesanstalt für Geowissenschaften und Rohstoffe*. <https://doi.org/10.25928/MBX6-HR74>
- Fukao, Y., & Obayashi, M. (2013). Subducted slabs stagnant above, penetrating through, and trapped below the 660 km discontinuity. *Journal of Geophysical Research: Solid Earth*, 118(11), 5920–5938. <https://doi.org/10.1002/2013JB010466>
- Gerstoft, P., & Bromirski, P. D. (2016). “Weather bomb” induced seismic signals. *Science*, 353(6302), 869–870. <https://doi.org/10.1126/science.aag1616>
- Gualtieri, L., Stutzmann, E., Farra, V., Capdeville, Y., Schimmel, M., Arduhin, F., & Morelli, A. (2014). Modelling the ocean site effect on seismic noise body waves. *Geophysical Journal International*, 197(2), 1096–1106. <https://doi.org/10.1093/gji/ggu042>
- Hasselmann, K. (1963). A statistical analysis of the generation of microseisms. *Reviews of Geophysics*, 1(2), 177–210. <https://doi.org/10.1029/RG001i002p00177>
- Hosseini, K., Sigloch, K., Tsekhmistrenko, M., Zaheri, A., Nissen-Meyer, T., & Igel, H. (2020). Global mantle structure from multifrequency tomography using P, PP and P-diffracted waves. *Geophysical Journal International*, 220(1), 96–141. <https://doi.org/10.1093/gji/ggz394>
- Kandilli Observatory And Earthquake Research Institute, Boğaziçi University. (1971). Kandilli Observatory and Earthquake Research Institute (KOERI). [Dataset]. *International Federation of Digital Seismograph Networks*. <https://doi.org/10.7914/SN/KO>
- Kato, S., & Nishida, K. (2023). Extraction of mantle discontinuities from teleseismic body-wave microseisms. *Geophysical Research Letters*, 50(18), e2023GL105017. <https://doi.org/10.1029/2023GL105017>
- Kennett, B., & Pham, T.-S. (2018). Evolution of the correlation wavefield extracted from seismic event coda. *Physics of the Earth and Planetary Interiors*, 282, 100–109. <https://doi.org/10.1016/j.pepi.2018.07.004>
- KNDC/Institute of Geophysical Research (Kazakhstan). (1994). Kazakhstan network [Dataset]. *International Federation of Digital Seismograph Networks*. <https://doi.org/10.7914/SN/KZ>

- Koelemeijer, P., Ritsema, J., Deuss, A., & Van Heijst, H.-J. (2016). SP12RTS: A degree-12 model of shear-and compressional-wave velocity for Earth's mantle. *Geophysical Journal International*, 204(2), 1024–1039. <https://doi.org/10.1093/gji/ggv481>
- Krischer, L., Megies, T., Barsch, R., Beyreuther, M., Lecocq, T., Caudron, C., & Wassermann, J. (2015). Obspy: A bridge for seismology into the scientific Python ecosystem. *Computational Science and Discovery*, 8(1), 014003. <https://doi.org/10.1088/1749-4699/8/1/014003>
- Lai, H., & Garnero, E. J. (2020). Travel time and waveform measurements of global multibounce seismic waves using virtual station seismogram stacks. *Geochemistry, Geophysics, Geosystems*, 21(1), e2019GC008679. <https://doi.org/10.1029/2019GC008679>
- Lay, T., Williams, Q., & Garnero, E. J. (1998). The core–mantle boundary layer and deep Earth dynamics. *Nature*, 392(6675), 461–468. <https://doi.org/10.1038/33083>
- Li, C., van der Hilst, R. D., Engdahl, E. R., & Burdick, S. (2008). A new global model for P wave speed variations in Earth's mantle. *Geochemistry, Geophysics, Geosystems*, 9(5), Q05018. <https://doi.org/10.1029/2007GC001806>
- Li, L., Boué, P., & Campillo, M. (2020). Observation and explanation of spurious seismic signals emerging in teleseismic noise correlations. *Solid Earth*, 11(1), 173–184. <https://doi.org/10.5194/se-11-173-2020>
- Li, L., Boué, P., Retaillé, L., & Campillo, M. (2020). Spatiotemporal correlation analysis of noise-derived seismic body waves with ocean wave climate and microseism sources. *Geochemistry, Geophysics, Geosystems*, 21(9), e2020GC009112. <https://doi.org/10.1029/2020GC009112>
- Longuet-Higgins, M. S. (1950). A theory of the origin of microseisms. *Philosophical Transactions of the Royal Society of London*, 243(857), 1–35. <https://doi.org/10.1098/rsta.1950.0012>
- Montelli, R., Nolet, G., Masters, G., Dahlen, F., & Hung, S.-H. (2004). Global P and PP traveltime tomography: Rays versus waves. *Geophysical Journal International*, 158(2), 637–654. <https://doi.org/10.1111/j.1365-246X.2004.02346.x>
- Nakata, N., Gualtieri, L., & Fichtner, A. (2019). *Seismic ambient noise*. Cambridge University Press.
- Nishida, K. (2013). Global propagation of body waves revealed by cross-correlation analysis of seismic hum. *Geophysical Research Letters*, 40(9), 1691–1696. <https://doi.org/10.1002/grl.50269>
- Nishida, K., & Takagi, R. (2016). Teleseismic S wave microseisms. *Science*, 353(6302), 919–921. <https://doi.org/10.1002/grl.50269>
- Nishida, K., & Takagi, R. (2022). A global centroid single force catalog of P-wave microseisms. *Journal of Geophysical Research*, 127(4), e2021JB023484. <https://doi.org/10.1029/2021JB023484>
- Nissen-Meyer, T., Fournier, A., & Dahlen, F. (2008). A 2-D spectral-element method for computing spherical-earth seismograms—II. Waves in solid–fluid media. *Geophysical Journal International*, 174(3), 873–888. <https://doi.org/10.1111/j.1365-246X.2008.03813.x>
- NOAA National Centers for Environmental Information. (2022). ETOPO 2022 15 Arc-Second Global Relief Model [Dataset]. *National Oceanic and Atmospheric Administration*. <https://doi.org/10.25921/fd45-gt74>
- Noubat, A., Brossier, R., Stehly, L., Cao, J., Paul, A., Team, C., & Group, A. W. (2023). Ambient-noise wave-equation tomography of the Alps and Ligurian-Provence basin. *Journal of Geophysical Research*, 128(10), e2023JB026776. <https://doi.org/10.1029/2023JB026776>
- Observatório Nacional, Rio de Janeiro, RJ. (2011). Rede sismográfica do sul e do sudeste [Dataset]. *International Federation of Digital Seismograph Networks*. <https://doi.org/10.7914/SN/ON>
- Pham, T.-S., Tkalcic, H., Sambridge, M., & Kennett, B. L. (2018). Earth's correlation wavefield: Late coda correlation. *Geophysical Research Letters*, 45(7), 3035–3042. <https://doi.org/10.1002/2018GL077244>
- Pinzon-Rincon, L., Lavoué, F., Mordret, A., Boué, P., Brenguier, F., Dales, P., et al. (2021). Humming trains in seismology: An opportune source for probing the shallow crust. *Seismological Research Letters*, 92(2A), 623–635. <https://doi.org/10.1785/0220200248>
- Poli, P., Campillo, M., Pedersen, H., & Group, L. W. (2012). Body-wave imaging of Earth's mantle discontinuities from ambient seismic noise. *Science*, 338(6110), 1063–1065. <https://doi.org/10.1126/science.1228194>
- Retaillé, L., Boué, P., Li, L., & Campillo, M. (2020). Ambient seismic noise imaging of the lowermost mantle beneath the North Atlantic Ocean. *Geophysical Journal International*, 222(2), 1339–1351. <https://doi.org/10.1093/gji/ggaa210>
- Rickett, J., & Claerbout, J. (1999). Acoustic daylight imaging via spectral factorization: Helioseismology and reservoir monitoring. *The Leading Edge*, 18(8), 957–960. <https://doi.org/10.1190/1.1438420>
- Ritsema, J., Deuss, A., Van Heijst, H., & Woodhouse, J. (2011). S40RTS: A degree-40 shear-velocity model for the mantle from new Rayleigh wave dispersion, teleseismic traveltime and normal-mode splitting function measurements. *Geophysical Journal International*, 184(3), 1223–1236. <https://doi.org/10.1111/j.1365-246X.2010.04884.x>
- Ritsema, J., Heijst, H. J. V., & Woodhouse, J. H. (1999). Complex shear wave velocity structure imaged beneath Africa and Iceland. *Science*, 286(5446), 1925–1928. <https://doi.org/10.1126/science.286.5446.1925>
- Ritsema, J., & Lekić, V. (2020). Heterogeneity of seismic wave velocity in Earth's mantle. *Annual Review of Earth and Planetary Sciences*, 48(1), 377–401. <https://doi.org/10.1146/annurev-earth-082119-065909>
- Romanowicz, B. (2003). Global mantle tomography: Progress status in the past 10 years. *Annual Review of Earth and Planetary Sciences*, 31(1), 303–328. <https://doi.org/10.1146/annurev-earth.31.091602.113555>
- Ruigrok, E., Draganov, D., & Wapenaar, K. (2008). Global-scale seismic interferometry: Theory and numerical examples. *Geophysical Prospecting*, 56(3), 395–417. <https://doi.org/10.1111/j.1365-2478.2008.00697.x>
- Russell, S., Rudge, J. F., Irving, J. C., & Cottaar, S. (2022). A re-examination of ellipticity corrections for seismic phases. *Geophysical Journal International*, 231(3), 2095–2101. <https://doi.org/10.1093/gji/ggac315>
- Sager, K., Boehm, C., Ermert, L., Krischer, L., & Fichtner, A. (2020). Global-scale full-waveform ambient noise inversion. *Journal of Geophysical Research*, 125(4), e2019JB018644. <https://doi.org/10.1029/2019JB018644>
- Sager, K., Tsai, V. C., Sheng, Y., Brenguier, F., Boué, P., Mordret, A., & Igel, H. (2022). Modelling P waves in seismic noise correlations: Advancing fault monitoring using train traffic sources. *Geophysical Journal International*, 228(3), 1556–1567. <https://doi.org/10.1093/gji/ggab389>
- Samantha, H. (2012). Transantarctic mountains Northern network. [Dataset]. *International Federation of Digital Seismograph Networks*. https://doi.org/10.7914/SN/ZI_2012
- Sanders, F., & Gyakum, J. R. (1980). Synoptic-dynamic climatology of the “bomb”. *Monthly Weather Review*, 108(10), 1589–1606. [https://doi.org/10.1175/1520-0493\(1980\)108%3C1589:SDCOT%3E2.0.CO;2](https://doi.org/10.1175/1520-0493(1980)108%3C1589:SDCOT%3E2.0.CO;2)
- Schimmel, M., & Paulsen, H. (1997). Noise reduction and detection of weak, coherent signals through phase-weighted stacks. *Geophysical Journal International*, 130(2), 497–505. <https://doi.org/10.1111/j.1365-246X.1997.tb05664.x>
- Shapiro, N. M., & Campillo, M. (2004). Emergence of broadband Rayleigh waves from correlations of the ambient seismic noise. *Geophysical Research Letters*, 31(7), L07614. <https://doi.org/10.1029/2004GL019491>
- Sheng, Y., Mordret, A., Sager, K., Brenguier, F., Boué, P., Rousset, B., et al. (2022). Monitoring seismic velocity changes across the San Jacinto Fault using train-generated seismic tremors. *Geophysical Research Letters*, 49(19), e2022GL098509. <https://doi.org/10.1029/2022GL098509>
- Tkalcic, H., & Pham, T.-S. (2018). Shear properties of Earth's inner core constrained by a detection of J waves in global correlation wavefield. *Science*, 362(6412), 329–332. <https://doi.org/10.1126/science.aau7649>

- Tkalčić, H., Pham, T.-S., & Wang, S. (2020). The Earth's coda correlation wavefield: Rise of the new paradigm and recent advances. *Earth-Science Reviews*, 208, 103285. <https://doi.org/10.1016/j.earscirev.2020.103285>
- Vinnik, L. (1973). Sources of microseismic *P* waves. *Pure and Applied Geophysics*, 103(1), 282–289. <https://doi.org/10.1007/BF00876404>
- Wapenaar, K., & Fokkema, J. (2006). Green's function representations for seismic interferometry. *Geophysics*, 71(4), SI33–SI46. <https://doi.org/10.1190/1.2213955>
- WW3DG. (2019). *User manual and system documentation of WAVEWATCH III version 6.07, the WAVEWATCH III development group* (Technical Note) (p. 326). NOAA/NWS/NCEP/MMAB. Appendices.
- Zaroli, C., Debayle, E., & Sambridge, M. (2010). Frequency-dependent effects on global *S*-wave traveltimes: Wavefront-healing, scattering and attenuation. *Geophysical Journal International*, 182(2), 1025–1042. <https://doi.org/10.1111/j.1365-246X.2010.04667.x>
- Zaroli, C., Lambotte, S., & Lévêque, J.-J. (2015). Joint inversion of normal-mode and finite-frequency *S*-wave data using an irregular tomographic grid. *Geophysical Supplements to the Monthly Notices of the Royal Astronomical Society*, 203(3), 1665–1681. <https://doi.org/10.1093/gji/ggv388>
- Zhang, R., Boué, P., Campillo, M., & Ma, J. (2023). Quantifying *P*-wave secondary microseisms events: A comparison of observed and modelled backprojection. *Geophysical Journal International*, 234(2), 933–947. <https://doi.org/10.1093/gji/ggad103>